HHS Public Access

Author manuscript

Clin Cancer Res. Author manuscript; available in PMC 2024 March 01.

Published in final edited form as:

Clin Cancer Res. 2023 September 01; 29(17): 3457–3470. doi:10.1158/1078-0432.CCR-22-2976.

Thyroid cancers exhibit oncogene-enhanced macropinocytosis that is restrained by IGF1R and promotes albumin-drug-conjugate response

Huiyu Hu[1,2,3], **Thomas S.C. Ng**[1,4], **Mikyung Kang**[1,4], **Ella Scott**[1], **Ran Li**[1,4], **Jeremy M. Quintana**[1,4], **Dylan Matvey**[1], **Venkata R. Vantaku**[2], **Ralph Weissleder**[1,4,5], **Sareh Parangi**[2], **Miles A. Miller**[1,4]

[1]Center for Systems Biology, Massachusetts General Hospital Research Institute, United States

[2]Department of Surgery, Massachusetts General Hospital and Harvard Medical School, United States

[3]Department of General Surgery, Xiangya Hospital, Central South University, China

[4]Department of Radiology, Massachusetts General Hospital and Harvard Medical School, United States

[5]Department of Systems Biology, Harvard Medical School, United States

Abstract

Purpose: Oncogene-driven macropinocytosis fuels nutrient scavenging in some cancer types, yet whether this occurs in thyroid cancers with prominent MAPK-ERK and PI3K pathway mutations remains unclear. We hypothesized that understanding links between thyroid cancer signaling and macropinocytosis might uncover new therapeutic strategies.

Experimental Design: Macropinocytosis was assessed across cells derived from papillary thyroid cancer (PTC), follicular thyroid cancer (FTC), non-malignant follicular thyroid, and aggressive anaplastic thyroid cancer (ATC), by imaging fluorescent dextran and serum albumin. The impacts of ectopic $BRAF^{V600E}$ and mutant *RAS*, genetic *PTEN* silencing, and inhibitors targeting RET, BRAF, and MEK kinases were quantified. $Braf^{V600E}$ $p53^{-/-}$ ATC tumors in immunocompetent mice were used to measure efficacy of an albumin-drug-conjugate comprising microtubule-destabilizing monomethyl auristatin E (MMAE) linked to serum albumin *via* a cathepsin-cleavable peptide (Alb-vc-MMAE).

Results: FTC and ATC cells showed greater macropinocytosis than non-malignant and PTC cells. ATC tumors accumulated albumin at 8.8% injected dose per gram tissue. Alb-vc-MMAE,

Corresponding authors: Sareh Parangi: Mailing address: 2014 Washington Street, Green Building, Suite 670, Newton MA 02462, Telephone number: 617-831-7798, sparangi@mgh.harvard.edu; Miles A. Miller: Mailing address: Center for Systems Biology, Massachusetts General Hospital, 185 Cambridge St, Boston, MA 02114. Telephone number: 617-643-0500, miles.miller@mgh.harvard.edu.

Conflict of interest statement:

RW is a co-founder of T2Biosystems and Lumicell, serves as a scientific advisor for ModeRNA Therapeutics, Tarveda Therapeutics, Accure Health, and Aikili Biosystems. MAM has served as a scientific advisor for January Therapeutics and has received research support from Pfizer, Genentech/Roche, and Ionis Pharmaceuticals. None of these activities relate to the manuscript. The other authors declare no competing interests.

but not MMAE alone, reduced tumor size by >90% ($P<0.01$). ATC macropinocytosis depended on MAPK/ERK activity and nutrient signaling, and increased by up to 230% with metformin, phenformin, or inhibition of insulin-like growth factor 1 receptor (IGF1Ri) in monoculture but not *in vivo*. Macrophages also accumulated albumin and express the cognate IGF1R ligand, IGF1, which reduced ATC responsiveness to IGF1Ri.

Conclusions: These findings identify regulated oncogene-driven macropinocytosis in thyroid cancers and demonstrate the potential of designing albumin-bound drugs to efficiently treat them.

Introduction

Dysfunctional vasculature and biosynthetic demands of proliferation can promote extracellular nutrient scavenging by malignant cells to sustain their survival and growth (1-4). Macropinocytosis is defined as the non-specific endocytic uptake of extracellular material by cells in a clathrin-independent manner and is recognized as a prominent scavenging pathway in cancers with oncogenic mutations that drive constitutive Ras GTPase or phosphoinositide 3-kinase (PI3K) pathway activities(1, 5, 6). These pathways stimulate the formation of cup-like structures on the cell surface that engulf extracellular fluid through membrane ruffling promoted by F-actin (7, 8). The structures collapse into macropinosomes that are shuttled into degradative endolysosomal vesicles. Rho family GTPases Rac1 and Cdc42 (9, 10), mammalian target of rapamycin (mTOR) and AMP-activated protein kinase (AMPK) signaling (11-13), mitogen activated protein kinase / extracellular related kinase (MAPK/ERK) activity (6), and other pathways have all been shown to regulate macropinocytosis in various contexts (14, 15).

In principle, constitutive cancer cell macropinocytosis offers a two-fold opportunity for therapeutic targeting of tumors. Since macropinocytosis mediates nutrient uptake, its inhibition has been shown to restrict cancer cell anabolism, proliferation, and resistance to biosynthesis-disrupting chemotherapies(16). On the other hand, macropinocytosis can promote tumor uptake of extracellular drugs that are bound to serum albumin or other proteins, encapsulated in nanoparticles, or are otherwise unable to transport across the plasma membrane of cells (6, 17-19). Nanoparticulate albumin bound paclitaxel (nab-paclitaxel, Abraxane) is one such drug that has been shown in mice to exhibit enhanced efficacy in a macropinocytosis-dependent manner (6).

Despite the diversity of mechanisms known to promote macropinocytosis in various cancer types, relatively little is known about the degree to which it occurs in thyroid cancers, and through which signaling pathways it may be controlled. Papillary thyroid carcinoma (PTC) comprises roughly 80% of all thyroid cancers and is characterized by a well-differentiated, localized phenotype and favorable clinical outcomes (20). Up to 50% of PTC harbors oncogenic mutations in *BRAF* (v-Raf murine sarcoma viral oncogene homolog B), most frequently via V600E mutation that drives constitutive RAF/MEK/ERK mitogenic signaling (21). 7-20% of PTC harbors a gene fusion involving the receptor tyrosine kinase RET, and such RET/PTC rearrangements promote constitutive MAPK/ERK activity (22). In contrast to PTC, follicular thyroid carcinoma (FTC) makes up 15% of all thyroid cancers and is more likely to contain mutations in *RAS* isoforms (*HRAS*, *NRAS*, and *KRAS*) rather than

in *BRAF* (23). Roughly 5% of FTC carries a mutation in the tumor suppressor *PTEN*, and up to 10% of individuals harboring germline *PTEN* mutation eventually develop FTC (24). *RAS* and *PTEN* mutations have both been shown to promote constitutive macropinocytosis in other cancer-types, including in pancreatic and prostate cancer, respectively, but little is known about such effects in thyroid cancer (1, 6, 13).

$BRAF^{V600E}$ associates with worse PTC outcomes (25) and is frequently found in anaplastic thyroid cancer (ATC)(26, 27), which is characterized by an aggressive undifferentiated phenotype. ATC constitutes <10% of all thyroid cancers but is responsible for up to half of all deaths (28). Combined inhibition of BRAF and downstream MEK1/2 kinases via dabrafenib and trametinib, respectively, show efficacy in treating patients with BRAF-mutant ATC (28); nonetheless, drug resistance remains common and better treatments are needed.

We hypothesized that dysregulated signaling driven by diverse oncogenic mutations, including $BRAF^{V600E}$, could promote constitutive thyroid cancer macropinocytosis. We further hypothesized this may be especially prominent in ATC, since aggressive cancers by nature exhibit high metabolic demands to fuel their proliferation. $BRAF^{V600E}$ is a common oncogenic driver mutation present across a variety of cancer-types beyond PTC and ATC, including melanoma, non-small-cell lung cancer, and colorectal cancer. Nonetheless, little is known about the potential role of mutant BRAF in regulating macropinocytosis. We find that various mutations — including $BRAF^{V600E}$, RET rearrangement, KRAS mutation, and PTEN loss — can promote macropinocytosis. Through *in vitro* and mouse allograft experiments, combined with analysis of bulk and single-cell RNA sequencing datasets from patients, this work establishes macropinocytosis as a metabolic signature of ATC that offers avenues for both treatment and monitoring.

Materials and Methods

Cell culture and materials.

Human cell lines, plasmids, siRNA, antibodies, sources and transfection details are listed in Supplementary Table S1. Murine TBP3743 (*TPO*-Cre^{ER}, $Braf^{tm1Mmcm/+}$, $Trp53^{tm1Brn/tm1Brn}$) ATC cells were as described (29). All were maintained in DMEM (Corning) with 10% FBS (Bio-Techne), 100 IU penicillin and 100 μg/mL streptomycin (Invitrogen), and routinely tested for mycoplasma (PCR, Applied Biological Materials). Lipofectamine 3000 (Invitrogen) and siRNA transfection reagent (Dharmacon) followed manufacturer protocols 72 h before macropinocytosis experiments in 96-well plates (Ibidi).

Fluorescent dye and drug conjugation.

Human serum albumin (HSA, Sigma) was conjugated to Alexa Fluor 555 (AF555) or AF647 via NHS-ester coupling, as previously (6). Drug-conjugate was synthesized by adding 125 μM of mouse serum albumin (MSA, Abcam) in PBS to equal volume 125 μM maleimide-valine-citrulline(vc)-MMAE (Selleck, 20% DMSO in PBS), stirring overnight at RT, and purifying with PBS via 3x 12,000g 5-minute centrifugation using 30kDa MWCO filters (Amicon). Macrin-VT680 nanoparticles were synthesized as prior (6, 30).

In vitro albumin and dextran uptake

5,000-10,000 cells per well were seeded overnight in 96-well plates (Ibidi). 1 μM HSA-AF647 or 100 μg/mL of 70kDa dextran labeled with TMR or fluorescein (Invitrogen) was then added for 4 h. Cells were washed with PBS, fixed (4% PFA, EMS), and counterstained (5 μg/mL DAPI, Sigma) before microscopy. In some experiments, cells were treated with drugs for 4-24 h (see Supplementary Table S2A) before adding HSA-AF647.

In vitro cytotoxicity

For MMAE and Alb-vc-MMAE, 3000 8505c or TBP3743 cells per well were seeded in 96-well plates (Corning) overnight. After 72 h treatment, cytotoxicity was assessed by PrestoBlue (Invitrogen). For assessing viability of adherent cells following dabrafenib and/or trametinib, 5000 TBP3743 cells per well were seeded overnight, treated for 24 h, stained with live/dead Viability/Cytotoxicity Kit (Thermo Scientific/Fisher) according to manufacturer's protocol, and immediately imaged.

Animal models.

Animal research was conducted in compliance with the Institutional Animal Care and Use Committee (IACUC) at MGH. Mice fed with autoclaved food and water were maintained in ventilated cages in a light-dark cycle, temperature and humidity-controlled pathogen-free environment. 5×10^5 TBP3743 in 5 μl PBS were injected into the right thyroid lobe of 6–10-week-old female B6129SF1/J mice (JAX), or 5×10^5 in 50 μl PBS were subcutaneously implanted in flanks. Tumor-free mice underwent sham surgery and PBS injection. 2.5% isoflurane with 2 L/min O_2 on a heated stage was used during injections; buprenorphine was used before and for 3 days after surgery.

In vivo drug-conjugate evaluation

9 days after tumor induction, mice were randomly assigned and treated with 1 μmol/kg MMAE (Selleck), 1 μmol/kg Alb-vc-MMAE, or vehicle through tail-vein injection. Tumor volumes ($V = 0.5 \times \text{length} \times \text{width}^2$) were by caliper, and pre-determined humane endpoints included ulceration, volumes >500 mm^3, and >20% body weight loss. Terminal cardiac puncture under anesthesia was used for MGH Veterinary Clinical Pathology Laboratory serum analysis. Livers underwent formalin fixation, paraffin embedding, sectioning, and hematoxylin and eosin staining, using the MGH Histopathology Core.

Biodistribution.

15 mg/kg HSA-AF647 and 15 mg/kg 70kDa dextran-TMR in 100 μl PBS, and 50 μl (1 mg/mL) of lectin-DyLight488 (Vector Laboratories) were tail-vein injected into tumor-bearing mice. 24 h after HSA/dextran and 30 min after lectin, mice were dissected following 20 mL PBS perfusion via cardiac puncture when anesthetized. Biodistribution used fluorescence reflectance imaging as prior (6). Where noted, animals received 1 mg/kg trametinib and/or 30 mg/kg dabrafenib in 1% methylcellulose via daily oral gavage, or 15 mg/kg AXL1717 in 10% DMSO and 90% olive oil, or 50 mg/kg metformin in PBS, via i.p. injection starting 1 d before HSA.

ATC cell and bone marrow-derived macrophage (BMDM) culture

Mouse BMDMs were from eight-week-old female B6129SF1/J as prior (31, 32). 15000 BMDM and/or 4000 TBP3743 were seeded overnight in 96-well plates (Ibidi), treated 2 h with Iscove's Modified Dulbecco's Medium (IMDM, Gibco) containing 10% FBS, P/S, 10 ng/mL murine M-CSF (Peprotech), and 500 nM AXL1717, 20 μg/ml anti-IGF1R mAb (R&D Systems), and/or vehicle. 5 μM of Macrin-VT680 (to mark macrophages)(32) and 1 μM HSA-AF555 were incubated for another 4 h before 4% PFA fixation.

Microscopy and flow cytometry.

Confocal microscopy used an FV1000 (Olympus) with ×20 XLUMPLFLN (NA0.95, Olympus) and filter sets as prior (6). *In vitro* microscopy used an IX81 (Olympus) (6). Fluorescence reflectance imaging used an OV110 (Olympus) (6). Liver histology used Nanozoomer (Hamamatsu). Flow cytometry followed prior protocols(33): minced tumors were digested with 1 mg/mL collagenase type I (Worthington) and type IV (Worthington), and 100 μg/mL DNase I (Sigma) in 1:2 ratio HBSS (Thermo Scientific/ Fisher) and RPMI1640 (Gibco) for 30 min, passed through 70 μm strainers (BD Falcon), and washed with RPMI1640. Rat anti-mouse CD16/CD32(RRID:AB_394656) and live/dead aqua (Thermo Scientific/Fisher) incubation in staining buffer was followed by CD45(RRID:AB_2565884), CD11b(RRID:AB_312793), and F4/80(RRID:AB_893477) staining, washing, and analysis on an Attune Cytometer (Thermo).

Immunoassays.

In siRNA experiments, 25 nM siRNA was treated to 500,000 8505c cells in 10 cm plates; 72 h later cells were treated and lysed in RIPA (Abcam) containing protease/phosphatase inhibitor cocktail (CST, #5872S)). Triplicates of 15 μg protein were resolved on 4-12% NuPAGE gels (Invitrogen) and transferred to nitrocellulose (Invitrogen). Membranes were incubated overnight at 4°C with antibodies for p-AMPK(RRID:AB_331250), p-IGF1R(RRID:AB_10548764), p-ERK1/2(RRID:AB_2315112), IGF1R(RRID:AB_10950969), AMPK(RRID:AB_490795), ERK(RRID:AB_390779), all 1:1000, or β-actin(RRID:AB_2242334) at 1:2000. Secondary antibodies with horseradish peroxidase (CST) stained 1 h at 1:2000, RT. Restore western blot stripping buffer (Thermo Scientific/Fisher) stripped membranes for 15 min. ECL Chemiluminescent substrate (Thermo Scientific/Fisher) was scanned (Azure Biosystems). Lysate IGF1 and total protein were measured by quantikine ELISA (R&D Systems) and Pierce BCA Protein Assay (Thermo), respectively.

In transient transfection experiments, after finishing imaging of HSA and dextran, cells were incubated with 4.5% H2O2 and 24 mM NaOH for 2h at RT under light exposure to bleach fluorescence following published CycIF protocols (34). 0.1% Triton-X100 (Sigma) was added for 10 min, followed by 1h incubation with 5% bovine serum albumin (BSA, Fisher Scientific) and 3% goat serum in PBS. Cells were incubated with p-ERK1/2(RRID:AB_2315112) or PTEN antibody (RRID:AB_390810) at 1:200 dilution in PBS containing 0.5% BSA, overnight at 4°C, washed in PBS containing 0.5% BSA, then incubated with 2 μg/mL anti-rabbit IgG AF647 (Invitrogen) in PBS containing 0.5% BSA for 2h before imaging.

Quantification and statistical analysis.

Image processing used Fiji v2.1.0 (NIH) and flow cytometry used FLowJo 10 (Becton Dickinson). Background-subtraction and normalization to control mean fluorescence was performed in some cases. Max/min window-level and acquisition parameters were applied consistently within experiments. In Figure 1, FTC cells were quantified in a separate cohort repeated with, normalized to, and windowed to Nthy-ori-3-1 uptake. Data are means ± standard error unless noted. Analyses were in Excel (Microsoft) or Prism 9.0 (GraphPad). P-values in captions used multiple hypothesis correction where noted and $\alpha = 0.05$. The ratio of fucodian inhibition to EIPA inhibition followed Δ fucoidan / Δ EIPA = $(mean_{control} - mean_{fucoidan}) / (mean_{control} - mean_{EIPA})$, after normalizing $mean_{control} = 1$ for the given experiment; standard error propagation assumed independence.

Bioinformatic analysis

Single-cell RNA seq (GSE148673)(35) was pooled across patients using published cell-type annotations, and SPRING was used for visualization (RRID:SCR_023578)(36). Myeloid scRNAseq was analyzed from the published scDVA browser (http://cancer-pku.cn:3838/CRC_Leukocyte/) (37). The Cancer Genome Atlas (TCGA, Firehose Legacy) database was analyzed using cBioPotal (RRID:SCR_014555, accessed 02-2023) (38). Mouse PTC and ATC gene expression data(GSE55933) (39), and shRNA screening data, were downloaded from the supplementary of the publications(40). WebGestalt (RRID:SCR_006786) (41)analyzed gene set enrichment with gene ID mapping (42) (Supplementary Table S2B-D).

Data Availability Statement

Data generated in this study are available from corresponding authors upon request. RNA sequencing and screening data were downloaded as described above (GSE148673, GSE55933, http://cancer-pku.cn:3838/CRC_Leukocyte/, and supplementary file download from the publication (40)).

Results

FTC, ATC, and some PTC cells exhibit upregulated macropinocytosis.

In vitro dextran uptake marks non-specific fluid-phase macropinocytosis in tumor cells (43), since carcinomas typically lack expression for receptor-mediated dextran endocytosis (44-46) (Fig. 1A-C). 1/2 PTC cell lines showed elevated dextran uptake compared to immortalized non-malignant follicular cells (Nthy-ori-3-1) (Fig. 1A-C). All FTC and ATC cell lines showed higher dextran uptake compared to PTC and Nthy-ori-3-1 cells. In ATC, punctate dextran consistent with macropinocytosis (Fig. 1D)(6, 13) reduced 66% when treated with EIPA (5-(N-ethyl-N-isopropyl)amiloride), which inhibits macropinocytosis (Supplementary Fig. S1A)(47).

Serum albumin is an abundant macropinocytosis substrate and an important vehicle for drug delivery (48). Fluorescent albumin was internalized by ATC cells, co-localized with co-administered dextran, and its uptake was similarly reduced 62% by EIPA (Fig. 1D-G). Both human ATC cells, and cells from a genetically engineered mouse model of $Braf^{V600E}$

p53$^{-/-}$ ATC (TBP3743 cells), showed EIPA-dependent uptake of albumin and dextran (Supplementary Fig. S1B). Co-imaging of albumin with geminin, which accumulates through S/G2/M cell-cycle phases, revealed slight dependence of albumin uptake on the cell-cycle (Supplementary Fig. S1C-D). Overall, macropinocytosis is consistently upregulated in FTC and ATC, and is a major uptake pathway of serum albumin in ATC.

ATC tumors accumulate albumin via macropinocytosis.

We assessed the degree to which macropinocytosis contributed to albumin uptake in ATC compared FTC, PTC, and follicular thyroid cells (Fig. 2A; Supplementary Fig. S1E). Albumin and dextran uptake did not correlate across cell lines ($P = 0.27$), and follicular thyroid cells surprisingly accumulated high albumin but low dextran (Fig. 2A). We hypothesized that receptor-mediated endocytosis might explain differences between dextran versus albumin uptake. Fucoidan is used to block receptor-mediated albumin endocytosis (49, 50), and we compared its effects with those of EIPA across follicular thyroid, PTC, and ATC cells (Fig. 2B, Supplementary Fig. S1F-I). In all cell lines, dextran uptake was reduced by EIPA but not fucoidan, indicating macropinocytosis. In contrast, fucoidan blocked albumin uptake as much as EIPA in follicular thyroid and PTC cells, indicating substantial receptor-mediated uptake. In ATC cells, albumin uptake was less affected by fucoidan than EIPA, therefore suggesting albumin uptake primarily through macropinocytosis in ATC.

We evaluated the degree to which ATC tumors accumulated albumin *in vivo*, compared to healthy thyroid. Albumin biodistribution was assessed 24h after intravenous injection, showing high orthotopic ATC allograft uptake of 8.8 percent injected dose per gram tissue (%ID/g) and a tumor : muscle uptake ratio of 27 : 1 (Fig. 2C-D). In contrast, healthy thyroids accumulated little albumin. Hepatic uptake was found and expected for albumin, which undergoes hepatic clearance (48). Compared to tumor-free mice, tumor-bearing mice showed increased albumin in the kidney, heart, and spleen (Fig. 2C-D). This data and hypoalbuminemia in tumor-bearing mice (Supplementary Fig. S2A) is possibly suggestive of systemic capillary leak, for instance arising from an altered systemic inflammation (51), and merits future investigation. Nonetheless, high tumor accumulation of albumin is consistent with constitutive macropinocytosis in ATC.

Treating ATC with the albumin-drug-conjugate Alb-vc-MMAE

We hypothesized albumin-bound chemotherapy may efficiently block ATC progression, since albumin accumulated in ATC within ranges seen for tumor-targeted antibodies (52) and nanotherapies exploiting the enhanced permeability and retention (EPR) effect (53) in other cancer-types. Microtubule-targeting paclitaxel is clinically used to treat ATC (28) but exhibits toxicities. To efficiently deliver microtubule-targeted drugs to ATC, we synthesized an albumin-drug-conjugate comprising the microtubule-destabilizing monomethyl auristatin E (MMAE) conjugated to serum albumin with a cathepsin-cleavable linker (Alb-vc-MMAE, Fig. 2D), and compared it to unconjugated MMAE. Albumin conjugation decreased MMAE cytotoxicity *in vitro,* consistent with conjugation stability over the 72h experiment: free MMAE is permeable and does not require slower, rate-limiting transport via macropinocytosis to reach its cytoplasmic target (Supplementary Fig. S2B)(54). However, *in vivo* free MMAE is rapidly cleared from the body, and we

hypothesized that macropinocytosis of Alb-vc-MMAE could promote activity via extended circulating pharmacokinetics and ATC macropinocytic uptake. Free MMAE showed no effect on ATC tumor growth, while equimolar Alb-vc-MMAE shrunk all tumors (>90% average volume decrease; Fig. 2E-G) and no substantial toxic effects by blood chemistry (albumin, alkaline phosphatase, alanine transaminase, glucose, bilirubin), liver histology, or weight loss were observed (Supplementary Fig. S2A, Supplementary Fig. S2C-E). Engineered albumin-binding improved responses in ATC tumors with high macropinocytosis activity.

MAPK/ERK signaling and PTEN loss contribute to macropinocytosis and albumin uptake.

We next examined how oncogenic mutations and phosphosignaling influence macropinocytosis in thyroid cancers. Transfection of follicular thyroid or $BRAF^{WT}$ PTC cells with $BRAF^{V600E}$ induced p-ERK1/2 and enhanced uptake of dextran and albumin (Fig. 3A-C; Supplementary Fig. S3A-B). To relate ERK activity with macropinocytosis on a cell-by-cell level, we generated a reporter $BRAF^{V600E}$ ATC cell line based on a fluorescent kinase translocation reporter (KTR) that accumulates in the cytoplasm or nucleus depending on whether its canonical ERK substrate is phosphorylated. The BRAF inhibitor dabrafenib, the MEK1/2 inhibitor trametinib, and their combination reduced both ERK activity and albumin uptake in ATC cells (Fig. 3D-F) that were confirmed as viable (Supplementary Fig. S3C-D). 0.5 μM dabrafenib incompletely blocked ERK activity and was less effective than 0.5 μM trametinib, despite similar biochemical potencies to their targets (~1 nM (55, 56)). This suggests potential dabrafenib-resistant ERK signaling, for instance through receptor tyrosine kinases and CRAF. Taken together, downstream MAPK/ERK pathway output controls ATC macropinocytosis.

We tested whether other prominent mutations in thyroid cancers could promote macropinocytosis. RET rearrangements stimulate MAPK/ERK signaling in PTC, and treating RET/PTC-expressing PTC cells with a kinase inhibitor targeting RET (pralsetinib) reduced p-ERK1/2 and decreased uptake of dextran and albumin by 20% and 24%, respectively (Fig. 3G-I). *RAS* mutations are common in FTC, and constitutively activated $KRAS^{G12D}$ promotes macropinocytosis in cancer-types including pancreatic adenocarcinoma (1, 6). Ectopic $KRAS^{G12D}$ enhanced p-ERK1/2 and dextran uptake compared to ectopic $KRAS^{WT}$ in follicular thyroid cells, but albumin uptake was not different (Supplementary Fig. S3E-G), indicating $KRAS^{G12D}$-promoted macropinocytosis and a distinct receptor-mediated albumin endocytosis response in these cells.

Since FTC cell lines showed elevated macropinocytosis, carried truncated loss-of-function *PTEN* mutation, but harbored no known *RAS* or *BRAF* mutation, we tested whether PTEN/PI3K perturbation could impact FTC macropinocytosis. Genetic *PTEN* silencing enhanced dextran and albumin uptake in follicular thyroid cells by 16% and 100%, respectively (Supplementary Fig. S3H-J). In FTC cells with PTEN loss, kinase inhibitors targeting PI3Kα (serabelisib and alpelisinib) showed mixed results: serabelisib reduced dextran uptake by 45% on average, but alpelisinib had no effect, despite its equimolar dose, similar potency, and shared mechanism (Supplementary Fig. S3K-N). Altogether, MAPK-ERK or

PI3K/PTEN dysregulation via diverse oncogenic mutations can promote macropinocytosis in thyroid cancers.

BRAF/MEK inhibition reduces macropinocytosis in cancer cells but not tumor-associated macrophages.

We next tested how targeted BRAF and MEK kinase inhibition of the MAPK-ERK pathway (MAPKi) could affect albumin macropinocytosis in ATC tumors. Tumor-bearing mice were treated with MAPKi 24h before intravenous injection of albumin, which reduced its uptake in malignant cells by 35% and correlated with decreased MAPK-ERK activity (Fig. 4A-C). Trametinib alone, and combined with dabrafenib, decreased albumin uptake in tumors but not other tissues (Fig. 4D, Supplementary Fig. S4A-B). MAPKi reduced average sizes of tumors and their albumin uptake, but lectin and dextran accumulation — as markers of functional tumor vasculature and phagocytic macrophages — did not change (Supplementary Fig. S4C-D). Thus, reduced albumin uptake was not merely due to a reduced ability to passively access tumor tissue.

Flow cytometry quantified how MAPKi affected partitioning of serum albumin within malignant and immune cell populations. 24h after albumin administration, tumors were digested into single-cell suspensions, immunostained for TAMs (CD45+ CD11b+ F4/80+), other myeloid cells (CD45+ CD11b+ F4/80-) and lymphocytes (CD45+ CD11b-) and quantified for cellular abundance and albumin uptake (Supplementary Fig. S4E-F). TAMs accumulated highest albumin on a per-cell basis (Supplementary Fig. S4F), consistent with confocal microscopy showing both malignant and especially phagocytic host cell uptake (57)(Fig. 4E). Nonetheless, most albumin within control-treated ATC tumors was found in malignant cells, since they were the most abundant cell-type (Fig. 4F-I). MAPKi decreased malignant cell uptake by 87% ($P < 0.01$; Fig. 4H), while TAM uptake was unchanged ($P = 0.63$; Fig. 4G). Treated tumors showed a greater relative TAM abundance ($P < 0.01$; Fig. 4I), and no difference was found by flow cytometry in overall cell viability following MAPKi (Supplementary Fig. S4G). MAPKi thus reduced albumin uptake in malignant ATC cells and shifted its relative accumulation to TAMs.

IGF1R inhibition augments albumin uptake but is blocked by IGF1.

We next examined potential mechanisms to further increase macropinocytosis in ATC. We analyzed hits from a genome-wide shRNA screen of bladder cancer macropinocytosis enhancement. The screen originally reported a gene-set enrichment of its 571 hits in KEGG signaling pathways including for insulin and MAPK (40); in a subsequent re-analysis, we found these and additional enrichment in pathways including for endocrine resistance, AMPK, FoxO, and RAS, at lower significance levels ($P<0.05$, but false-discovery-rate adjusted $q>0.05$)(Supplementary Table S2B-D). We also found high-ranking enrichment in disease-associated gene-sets, including for “body weight” and “impaired glucose tolerance” (Supplementary Table S2B-D). We tabulated RNA expression of the top 105 screen hits (40) among 397 PTC samples in the Cancer Genome Atlas (TCGA), and found insulin-like growth factor 1 receptor (IGF1R) as the 3rd highest hit based on median expression (Fig. 5A; Supplementary Table S2E). To investigate these pathways in ATC macropinocytosis, we performed a targeted pharmacologic screen to assess how 17 different compounds affected

ATC albumin uptake (Fig. 5B-C) using phenformin and metformin as agents known to activate AMPK; 2-deoxy-D-glucose (2DG), lonidamine, and 3-bromopyruvate (3BP) as glycolysis disrupting agents; oxythiamine as an antimetabolite transketolase inhibitor; 6-diazo-5-oxo-L-norleucine (DON), BPTES and V9302 as compounds modulating glutamine; and several targeted kinase inhibitors, including linsitinib and AXL1717/picropodophyllin as compounds inhibiting IGF1R (Supplementary Table S2A). Metformin, phenformin, and inhibitors targeting IGF1R were the only agents to consistently enhance albumin uptake across both human and mouse ATC cells (Fig. 5B-C). Combined AXL1717 and metformin did not elicit greater effects compared to single-agent treatments, potentially suggesting overlapping effects (Fig. 5D).

AXL1717 and/or metformin failed to affect bulk tumor accumulation of albumin in ATC (Fig. 5E), and we investigated the disparity between monoculture and *in vivo* results. IGF1R silencing using siRNA in ATC cells reduced IGF1R and its phosphorylation to undetectable levels, and increased both albumin and dextran uptake (Fig. 5F-G, Supplementary Fig. S5A-B). IGF1R siRNA did not further enhance the effects of AXL1717 on macropinocytosis, and AXL1717 slightly decreased basal p-IGF1R (Fig. 5G-H, Supplementary Fig. S5A-C). These data support basal IGF1R signaling as suppressing macropinocytosis in ATC monoculture.

We hypothesized ATC response *in vivo* could be affected by growth factors supplied by other cells in the tumor microenvironment. Macrophage-derived insulin-like growth factor 1 (IGF1) has been reported as redirecting phagocytosis in other contexts (58), and we detected IGF1 in ATC tumors (Supplementary Fig. S5D). Therefore, we tested whether IGF1 addition could block effects of IGF1R inhibition. AXL1717 and IGF1R siRNA treatments failed to enhance macropinocytosis in ATC cells in the presence of recombinant IGF1, which is known to bind both IGF1R and insulin receptor (Fig. 5F). AXL1717 failed to reduce exogenous IGF1-stimulated IGF1R phosphorylation (Fig. 5G-H), and published data show AXL1717 only partially inhibits IGF-stimulated p-IGF1R in other cancer-types (59). IGF1 treatment decreased p-AMPK regardless of AXL1717 or siRNA treatment (Fig. 5I, Supplementary Fig. S5C). In effect, IGF1 neutralized the ability of IGF1R inhibition to enhance macropinocytosis in ATC.

Macrophages modulate IGF1R signaling to affect albumin uptake in ATC.

We analyzed possible sources of IGF1 signaling in thyroid cancers. From bulk tissue, IGF1R protein and mRNA levels in TCGA data revealed IGF1R levels were 2-fold higher in BRAF-mutant compared to BRAF-wildtype thyroid tumors (Supplementary Fig. S5E-F). *IGF1* was expressed at lower levels than *IGF1R*, and did not correlate with BRAF mutation (Supplementary Fig. S5G-H). In genetically engineered mouse models, *Igf1r* and *Igf1* were both highly expressed in *Braf*-mutant PTC and ATC tumors (Supplementary Fig. S5I). *IGF1* and *IGF1R* expression in ATC tumors from five patients, using published single-cell RNA sequencing (scRNA-seq) (35), revealed both malignant and myeloid cell populations expressed *IGF1*, particularly among myeloid cells exhibiting M2-like macrophage gene expression patterns (CD206+ cells in ATC consistent with C1QC+ macrophages identified in thyroid cancer and other cancer types) (Fig. 6A-B, Supplementary Fig. S6)(37). In contrast, *IGF1R* was more highly expressed in malignant but not myeloid cells in ATC and

other cancer-types (Fig. 6C-D, Supplementary Fig. S6). *IGF1R* is thus highly expressed in BRAF-mutant thyroid cancers including ATC, and mixed *IGF1* expression is detected in both malignant and myeloid cells within the ATC tumor microenvironment.

To assess whether TAMs could directly influence IGF1R-dependent ATC macropinocytosis, we co-cultured IL4-polarized bone marrow-derived macrophages (IL4 BMDMs, known to express CD206(32) and IGF1(60)) with murine ATC (TBP3743) cells. AXL1717 and an IGF1R-blocking antibody, both separately and in combination, increased albumin uptake more in TBP3743 monoculture than in BMDM co-culture (Fig. 6E). These data show how IGF1, macrophages, and potentially other macrophage-supplied signaling factors influence ATC macropinocytosis to suppress the effects of IGF1R inhibition (Fig. 6F).

Discussion

Thyroid cancer often carries MAPK/ERK and PI3K pathway mutations and is the fifth most common cancer in women worldwide, but little has been described about macropinocytosis in this disease. Here, we identified elevated constitutive macropinocytosis in 5/5 combined FTC and ATC cell lines tested, but macropinocytosis was lower and more variable in the two PTC cells tested. We focused particularly on aggressive $BRAF^{V600E}$ ATC, and treatment with kinase inhibitors targeting BRAF or MEK reduced macropinocytosis in BRAF-mutant ATC. ATC accumulated serum albumin via macropinocytosis, syngeneic ATC tumors in mice accumulated >30-fold greater albumin than healthy thyroid, and combined BRAF and MEK inhibition reduced macropinocytosis in cancer cells but not macrophages or other tumor-associated leukocytes. Macropinocytic albumin uptake thus depended on $BRAF^{V600E}$-driven MAPK/ERK activity in ATC, and these data raise questions about whether $BRAF^{V600E}$ similarly promotes macropinocytosis in other cancer-types where $BRAF^{V600E}$ is common.

Despite our focus on $BRAF^{V600E}$, its presence or absence was not the sole determinant of macropinocytosis in thyroid cancer. Ectopic $BRAF^{V600E}$ stimulated macropinocytosis in follicular thyroid cells, but the mere existence of $BRAF^{V600E}$ failed to induce macropinocytosis in $BRAF^{V600E}$ BCPAP PTC cells. BCPAP are reported to exhibit lower constitutive p-ERK1/2 compared to the more aggressive $BRAF^{V600E}$ ATC cell lines studied here (61). Although this suggests downstream MAPK/ERK output correlates with macropinocytosis, we found counter-examples in comparing RET/PTC versus BRAF-mutant PTC. $BRAF^{V600E}$ associates with higher MAPK/ERK activity than as promoted by RET rearrangement in PTC (62), but TPC1 cells harboring RET fusion exhibited higher macropinocytosis than BCPAP, suggesting additional regulatory factors. In contrast to PTC, FTC frequently harbors *RAS* and *PTEN* mutations (23-24), and we found that both *PTEN* silencing and ectopic mutant *KRAS* could promote macropinocytosis in follicular thyroid cells. Taken together, we found consistent macropinocytosis in FTC and ATC, promoted through diverse routes of phosphosignaling dysregulation.

ATC accumulated high levels of serum albumin by macropinocytosis, and such albumin uptake can serve as an amino acid nutrient source in RAS-mutant cancers including $KRAS^{G12D}$ pancreatic adenocarcinoma (1-6); nonetheless, multiple mechanisms beyond

macropinocytosis govern serum albumin transport and uptake throughout the body, including via receptor-mediated endocytosis, transcytosis, and FcRn (neonatal Fc receptor) recycling. Both class A and class B scavenger receptors can mediate the uptake or transcytosis of albumin and chemically modified versions thereof (48). Comparing the effects of fucoidan with EIPA showed how multiple routes of albumin transport explain the imperfect correlation between cellular accumulation of dextran compared to albumin across thyroid cells, and reinforced macropinocytosis as a prominent uptake pathway in ATC (Fig. 2A-B). *In vivo*, nonspecific convection/diffusion processes, including factors of enhanced permeability and retention (EPR) seen heterogeneously in patients, also influence the transport of albumin and other macropinocytosis substrates. Comparing albumin uptake in the normal thyroid with uptake in ATC, along with multichannel imaging and flow cytometry of the ATC tumor microenvironment, all showed data consistent with cancer cell macropinocytosis as a key driver of albumin tumor accumulation.

Constitutive macropinocytosis has been therapeutically targeted as a pathway that supports malignant cell survival and proliferation (1-4), and here we demonstrate that clinically used BRAF and MEK kinase inhibitor therapy efficiently downregulates macropinocytosis in ATC. Future studies may more closely examine mechanisms of how MAPK/ERK inhibition impacts F-actin dynamics to limit macropinocytosis at the cell surface and may consider strategies to capitalize on potential drug sensitivities created by reduced macropinocytosis. On the other hand, high macropinocytosis may promote the delivery of highly albumin-bound, nanoparticle-based, or otherwise cell impermeable therapies that rely on macropinocytosis for their delivery (6, 17-19). As a proof of principle, we demonstrated how covalent albumin-binding of the chemotherapy MMAE enhanced efficacy in treating ATC allografts; such albumin conjugation confers advantages in extending the circulating pharmacokinetic half-life of its therapeutic payload, and facilitates tumor uptake through factors including EPR effects and macropinocytosis. $BRAF^{V600E}$-driven macropinocytosis may thus facilitate more efficient drug delivery while minimizing off-target uptake and toxicity. This result motivates future studies to quantify the degree to which macropinocytosis occurs in ATC patients, for instance via radiologic imaging of albumin uptake by positron emission tomography (PET)(48, 63), or by histologic assessment of labeled albumin uptake during tumor resection(64). Such studies may inform biomarker strategies to predict patients likely to respond to macropinocytosis-dependent therapy.

Supplementary Material

Refer to Web version on PubMed Central for supplementary material.

Acknowledgements

This work was supported in part by NIH grants DP2CA259675 (M.Miller), R00CA207744 (M.Miller), T32CA079443 (J.Quintana), U01CA206997 (R.Weissleder), R01GM138790 (M.Miller), and the President and Fellows of Harvard College (S.Parangi). H.Hu was supported by the China Scholarship Council 201906370164. M. Kang received support from the National Research Foundation of S. Korea. R.Li was supported in part by American Cancer Society Postdoctoral Fellowship PF-20-106-01-LIB. The authors are grateful to Dr. Michelle A. Garlin, Yoshiko Iwamoto and the MGH Histopathology Research Core for assistance with liver histology, Gregory Wojtkiewicz for assistance through the MGH-CSB MIP program.

Glossary

HSA	Human serum albumin
EPR	Enhanced permeability and retention
TME	Tumor microenvironment
AMPK	AMP-activated protein kinase
MAPK/ERK	Mitogen-activated protein kinase/extracellular signal-regulated kinase
BRAF	v-Raf murine sarcoma viral oncogene homolog B
KRAS	Kirsten rat sarcoma virus
TAM	Tumor associated macrophage

Reference:

1. Commisso C, Davidson SM, Soydaner-Azeloglu RG et al. Macropinocytosis of protein is an amino acid supply route in Ras-transformed cells. Nature. 2013;497:633–7. [PubMed: 23665962]
2. Kamphorst JJ, Nofal M, Commisso C et al. Human pancreatic cancer tumors are nutrient poor and tumor cells actively scavenge extracellular protein. Cancer Res. 2015;75:544–53. [PubMed: 25644265]
3. Guo JY, Teng X, Laddha SV et al. Autophagy provides metabolic substrates to maintain energy charge and nucleotide pools in Ras-driven lung cancer cells. Genes Dev. 2016;30:1704–17. [PubMed: 27516533]
4. Zhang MS, Cui JD, Lee D et al. Hypoxia-induced macropinocytosis represents a metabolic route for liver cancer. Nat Commun. 2022;13:954. [PubMed: 35177645]
5. Davidson SM, Jonas O, Keibler MA et al. Direct evidence for cancer-cell-autonomous extracellular protein catabolism in pancreatic tumors. Nat Med. 2017;23:235–41. [PubMed: 28024083]
6. Li R, Ng TSC, Wang SJ et al. Therapeutically reprogrammed nutrient signalling enhances nanoparticulate albumin bound drug uptake and efficacy in KRAS-mutant cancer. Nat Nanotechnol. 2021;16:830–9. [PubMed: 33958764]
7. Kay RR, Williams TD, Paschke P. Amplification of PIP3 signalling by macropinocytic cups. Biochem J. 2018;475:643–8. [PubMed: 29444849]
8. Veltman DM, Lemieux MG, Knecht DA, Insall RH. PIP_3-dependent macropinocytosis is incompatible with chemotaxis. J Cell Biol. 2014;204:497–505. [PubMed: 24535823]
9. Garrett WS, Chen LM, Kroschewski R et al. Developmental control of endocytosis in dendritic cells by Cdc42. Cell. 2000;102:325–34. [PubMed: 10975523]
10. West MA, Prescott AR, Eskelinen EL, Ridley AJ, Watts C. Rac is required for constitutive macropinocytosis by dendritic cells but does not control its downregulation. Curr Biol. 2000;10:839–48. [PubMed: 10899002]
11. Palm W, Park Y, Wright K, Pavlova NN, Tuveson DA, Thompson CB. The Utilization of Extracellular Proteins as Nutrients Is Suppressed by mTORC1. Cell. 2015;162:259–70. [PubMed: 26144316]
12. Nofal M, Zhang K, Han S, Rabinowitz JD. mTOR Inhibition Restores Amino Acid Balance in Cells Dependent on Catabolism of Extracellular Protein. Mol Cell. 2017;67:936–946.e5. [PubMed: 28918901]
13. Kim SM, Nguyen TT, Ravi A et al. PTEN Deficiency and AMPK Activation Promote Nutrient Scavenging and Anabolism in Prostate Cancer Cells. Cancer Discov. 2018;8:866–83. [PubMed: 29572236]

14. Su H, Yang F, Fu R et al. Cancer cells escape autophagy inhibition via NRF2-induced macropinocytosis. Cancer Cell. 2021;39:678–693.e11. [PubMed: 33740421]
15. Lee SW, Zhang Y, Jung M, Cruz N, Alas B, Commisso C. EGFR-Pak Signaling Selectively Regulates Glutamine Deprivation-Induced Macropinocytosis. Dev Cell. 2019;50:381–392.e5. [PubMed: 31257175]
16. Jayashankar V, Edinger AL. Macropinocytosis confers resistance to therapies targeting cancer anabolism. Nat Commun. 2020;11:1121. [PubMed: 32111826]
17. Liu H, Sun M, Liu Z et al. KRAS-enhanced macropinocytosis and reduced FcRn-mediated recycling sensitize pancreatic cancer to albumin-conjugated drugs. J Control Release. 2019;296:40–53. [PubMed: 30653981]
18. Desai AS, Hunter MR, Kapustin AN. Using macropinocytosis for intracellular delivery of therapeutic nucleic acids to tumour cells. Philos Trans R Soc Lond B Biol Sci. 2019;374:20180156. [PubMed: 30967005]
19. Colin M, Delporte C, Janky R et al. Dysregulation of Macropinocytosis Processes in Glioblastomas May Be Exploited to Increase Intracellular Anti-Cancer Drug Levels: The Example of Temozolomide. Cancers (Basel). 2019;11:E411.
20. LeClair K, Bell KJL, Furuya-Kanamori L, Doi SA, Francis DO, Davies L. Evaluation of Gender Inequity in Thyroid Cancer Diagnosis: Differences by Sex in US Thyroid Cancer Incidence Compared With a Meta-analysis of Subclinical Thyroid Cancer Rates at Autopsy. JAMA Intern Med. 2021;181:1351–8. [PubMed: 34459841]
21. Cantwell-Dorris ER, O'Leary JJ, Sheils OM. BRAFV600E: implications for carcinogenesis and molecular therapy. Mol Cancer Ther. 2011;10:385–94. [PubMed: 21388974]
22. Mitsutake N, Miyagishi M, Mitsutake S et al. BRAF mediates RET/PTC-induced mitogen-activated protein kinase activation in thyroid cells: functional support for requirement of the RET/PTC-RAS-BRAF pathway in papillary thyroid carcinogenesis. Endocrinology. 2006;147:1014–9. [PubMed: 16254036]
23. Xing M. Clinical utility of RAS mutations in thyroid cancer: a blurred picture now emerging clearer. BMC Med. 2016;14:12. [PubMed: 26817707]
24. Nagy R, Ganapathi S, Comeras I et al. Frequency of germline PTEN mutations in differentiated thyroid cancer. Thyroid. 2011;21:505–10. [PubMed: 21417916]
25. Kebebew E, Weng J, Bauer J et al. The prevalence and prognostic value of BRAF mutation in thyroid cancer. Ann Surg. 2007;246:466–70; discussion 470. [PubMed: 17717450]
26. Woodward EL, Biloglav A, Ravi N et al. Genomic complexity and targeted genes in anaplastic thyroid cancer cell lines. Endocr Relat Cancer. 2017;24:209–20. [PubMed: 28235956]
27. Landa I, Pozdeyev N, Korch C et al. Comprehensive Genetic Characterization of Human Thyroid Cancer Cell Lines: A Validated Panel for Preclinical Studies. Clin Cancer Res. 2019;25:3141–51. [PubMed: 30737244]
28. Bible KC, Kebebew E, Brierley J et al. 2021 American Thyroid Association Guidelines for Management of Patients with Anaplastic Thyroid Cancer. Thyroid. 2021;31:337–86. [PubMed: 33728999]
29. Vanden Borre P, McFadden DG, Gunda V et al. The next generation of orthotopic thyroid cancer models: immunocompetent orthotopic mouse models of BRAF V600E-positive papillary and anaplastic thyroid carcinoma. Thyroid. 2014;24:705–14. [PubMed: 24295207]
30. Kim HY, Li R, Ng TSC et al. Quantitative Imaging of Tumor-Associated Macrophages and Their Response to Therapy Using 64Cu-Labeled Macrin. ACS Nano. 2018;12:12015–29. [PubMed: 30508377]
31. Choo YW, Kang M, Kim HY et al. M1 Macrophage-Derived Nanovesicles Potentiate the Anticancer Efficacy of Immune Checkpoint Inhibitors. ACS Nano. 2018;12:8977–93. [PubMed: 30133260]
32. Luthria G, Li R, Wang S et al. In vivo microscopy reveals macrophage polarization locally promotes coherent microtubule dynamics in migrating cancer cells. Nat Commun. 2020;11:3521. [PubMed: 32665556]

33. Oh J, Carlson JCT, Landeros C et al. Rapid Serial Immunoprofiling of the Tumor Immune Microenvironment by Fine Needle Sampling. Clin Cancer Res. 2021;27:4781–93. [PubMed: 34233961]
34. Lin JR, Fallahi-Sichani M, Sorger PK. Highly multiplexed imaging of single cells using a high-throughput cyclic immunofluorescence method. Nat Commun. 2015;6:8390. [PubMed: 26399630]
35. Gao R, Bai S, Henderson YC et al. Delineating copy number and clonal substructure in human tumors from single-cell transcriptomes. Nat Biotechnol. 2021;39:599–608. [PubMed: 33462507]
36. Weinreb C, Wolock S, Klein AM. SPRING: a kinetic interface for visualizing high dimensional single-cell expression data. Bioinformatics. 2018;34:1246–8. [PubMed: 29228172]
37. Cheng S, Li Z, Gao R et al. A pan-cancer single-cell transcriptional atlas of tumor infiltrating myeloid cells. Cell. 2021;184:792–809.e23. [PubMed: 33545035]
38. Cerami E, Gao J, Dogrusoz U et al. The cBio cancer genomics portal: an open platform for exploring multidimensional cancer genomics data. Cancer Discov. 2012;2:401–4. [PubMed: 22588877]
39. McFadden DG, Vernon A, Santiago PM et al. p53 constrains progression to anaplastic thyroid carcinoma in a Braf-mutant mouse model of papillary thyroid cancer. Proc Natl Acad Sci U S A. 2014;111:E1600–9. [PubMed: 24711431]
40. Redelman-Sidi G, Binyamin A, Gaeta I et al. The Canonical Wnt Pathway Drives Macropinocytosis in Cancer. Cancer Res. 2018;78:4658–70. [PubMed: 29871936]
41. Liao Y, Wang J, Jaehnig EJ, Shi Z, Zhang B. WebGestalt 2019: gene set analysis toolkit with revamped UIs and APIs. Nucleic Acids Res. 2019;47:W199–205. [PubMed: 31114916]
42. Koopmans F, van Nierop P, Andres-Alonso M et al. SynGO: An Evidence-Based, Expert-Curated Knowledge Base for the Synapse. Neuron. 2019;103:217–234.e4. [PubMed: 31171447]
43. Commisso C, Flinn RJ, Bar-Sagi D. Determining the macropinocytic index of cells through a quantitative image-based assay. Nat Protoc. 2014;9:182–92. [PubMed: 24385148]
44. Sallusto F, Cella M, Danieli C, Lanzavecchia A. Dendritic cells use macropinocytosis and the mannose receptor to concentrate macromolecules in the major histocompatibility complex class II compartment: downregulation by cytokines and bacterial products. J Exp Med. 1995;182:389–400. [PubMed: 7629501]
45. Kato M, Neil TK, Fearnley DB, McLellan AD, Vuckovic S, Hart DN. Expression of multilectin receptors and comparative FITC-dextran uptake by human dendritic cells. Int Immunol. 2000;12:1511–9. [PubMed: 11058570]
46. Pustylnikov S, Sagar D, Jain P, Khan ZK. Targeting the C-type lectins-mediated host-pathogen interactions with dextran. J Pharm Pharm Sci. 2014;17:371–92. [PubMed: 25224349]
47. Koivusalo M, Welch C, Hayashi H et al. Amiloride inhibits macropinocytosis by lowering submembranous pH and preventing Rac1 and Cdc42 signaling. J Cell Biol. 2010;188:547–63. [PubMed: 20156964]
48. Hu H, Quintana J, Weissleder R, Parangi S, Miller M. Deciphering albumin-directed drug delivery by imaging. Adv Drug Deliv Rev. 2022;185:114237. [PubMed: 35364124]
49. Wang R, Chandawarkar RY. Phagocytosis of fungal agents and yeast via macrophage cell surface scavenger receptors. J Surg Res. 2010;164:e273–9. [PubMed: 20888598]
50. Miao L, Lin J, Huang Y et al. Synergistic lipid compositions for albumin receptor mediated delivery of mRNA to the liver. Nat Commun. 2020;11:2424. [PubMed: 32415122]
51. Soeters PB, Wolfe RR, Shenkin A. Hypoalbuminemia: Pathogenesis and Clinical Significance. JPEN J Parenter Enteral Nutr. 2019;43:181–93. [PubMed: 30288759]
52. Thurber GM, Schmidt MM, Wittrup KD. Antibody tumor penetration: transport opposed by systemic and antigen-mediated clearance. Adv Drug Deliv Rev. 2008;60:1421–34. [PubMed: 18541331]
53. Wilhelm S, Tavares AJ, Dai Q et al. Analysis of nanoparticle delivery to tumours. Nature reviews materials. 2016;1:1–12.
54. Li F, Emmerton KK, Jonas M et al. Intracellular Released Payload Influences Potency and Bystander-Killing Effects of Antibody-Drug Conjugates in Preclinical Models. Cancer Res. 2016;76:2710–9. [PubMed: 26921341]

55. Menzies AM, Long GV, Murali R. Dabrafenib and its potential for the treatment of metastatic melanoma. Drug Des Devel Ther. 2012;6:391–405.
56. Yamaguchi T, Kakefuda R, Tanimoto A, Watanabe Y, Tajima N. Suppressive effect of an orally active MEK1/2 inhibitor in two different animal models for rheumatoid arthritis: a comparison with leflunomide. Inflamm Res. 2012;61:445–54. [PubMed: 22245957]
57. Weissleder R, Nahrendorf M, Pittet MJ. Imaging macrophages with nanoparticles. Nat Mater. 2014;13:125–38. [PubMed: 24452356]
58. Han CZ, Juncadella IJ, Kinchen JM et al. Macrophages redirect phagocytosis by non-professional phagocytes and influence inflammation. Nature. 2016;539:570–4. [PubMed: 27820945]
59. Girnita A, Girnita L, del Prete F, Bartolazzi A, Larsson O, Axelson M. Cyclolignans as inhibitors of the insulin-like growth factor-1 receptor and malignant cell growth. Cancer Res. 2004;64:236–42. [PubMed: 14729630]
60. Barrett JP, Minogue AM, Falvey A, Lynch MA. Involvement of IGF-1 and Akt in M1/M2 activation state in bone marrow-derived macrophages. Exp Cell Res. 2015;335:258–68. [PubMed: 26022664]
61. Vanden Borre P, Gunda V, McFadden DG et al. Combined BRAF(V600E)- and SRC-inhibition induces apoptosis, evokes an immune response and reduces tumor growth in an immunocompetent orthotopic mouse model of anaplastic thyroid cancer. Oncotarget. 2014;5:3996–4010. [PubMed: 24994118]
62. Network CGAR. Integrated genomic characterization of papillary thyroid carcinoma. Cell. 2014;159:676–90. [PubMed: 25417114]
63. Niu G, Lang L, Kiesewetter DO et al. In Vivo Labeling of Serum Albumin for PET. J Nucl Med. 2014;55:1150–6. [PubMed: 24842890]
64. Wang Z, Chen M, Liu JJ et al. Human Serum Albumin Decorated Indocyanine Green Improves Fluorescence-Guided Resection of Residual Lesions of Breast Cancer in Mice. Front Oncol. 2021;11:614050. [PubMed: 33763353]
65. Otto GP, Rathkolb B, Oestereicher MA et al. Clinical Chemistry Reference Intervals for C57BL/6J, C57BL/6N, and C3HeB/FeJ Mice (Mus musculus). J Am Assoc Lab Anim Sci. 2016;55:375–86. [PubMed: 27423143]
66. Bankert RB, Mazzaferro PK Biochemistry of Immunoglobulins. In: Loeb WF, Quimby FW, editors. The clinical chemistry of laboratory animals. 2nd, ed. Taylor and Francis; Philadelphia: 1999. pp. 231–265.

Translational Relevance

Macropinocytosis is a non-specific, physiologically regulated process through which extracellular material is engulfed by ruffling of the cell membrane into cup-like structures. As recently recognized, a growing diversity of cancer types constitutively upregulate macropinocytosis to scavenge nutrients, including through dysregulated MAPK-ERK and PI3K signaling. We hypothesized that prominent signaling pathway mutations in thyroid cancers could stimulate macropinocytosis in these cells, offering a route to selective drug delivery, particularly in aggressive and often treatment-refractory anaplastic thyroid cancer (ATC). Through in vitro experiments, genetically engineered mouse model imaging, and patient-derived dataset analysis, we identify oncogene-driven macropinocytosis in follicular and anaplastic thyroid cancers, and uncover its regulation by $BRAF^{V600E}$ and insulin-like growth factor 1 receptor (IGF1R) in ATC. As a strategy to target this process, we synthesized an albumin-drug-conjugate that accumulates in macropinocytic ATC tumors and blocks tumor growth.

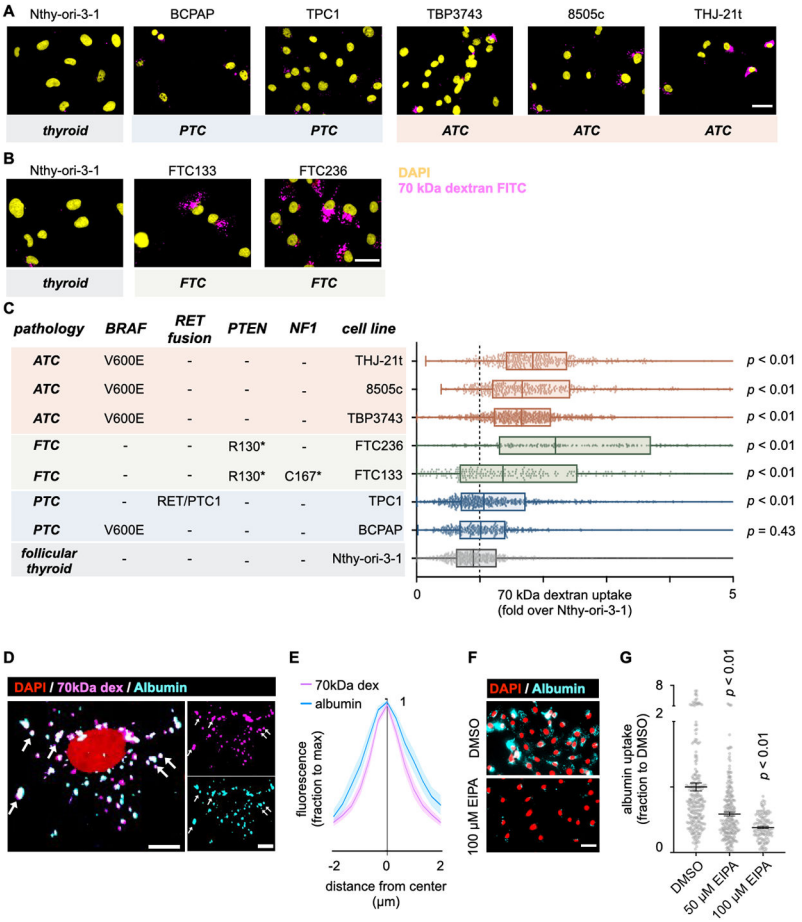

Figure 1. Thyroid cancer cells exhibit constitutive macropinocytosis and accumulate serum albumin.

Representative images (**A-B**, scale bar, 50μm) and quantification (**C**) of the uptake of 70kDa fluorescent dextran after 4h incubation in live papillary thyroid cancer (PTC) and anaplastic thyroid cancer (ATC) cells (**A**) or follicular thyroid cancer (FTC) cells (**B**). Corresponding image quantification (**C**) is shown as medians ± interquartile range, using one-way ANOVA/ Dunnett tests compared to Nthy-ori-3-1 (n≥ 246 cells). **D**, Representative microscopy of dextran and human serum albumin in 8505c ATC cells (scale bar, 10μm, arrows highlight punctate co-localization). **E**, Co-localized distribution of dextran (magenta) and serum albumin (cyan) in 8505c cells, quantified across individual ~2μm puncta (data are means ± s.e., n=27 images). **F-G**, Representative images (**F**, scale bar, 50μm) and quantification (**G**) of 4h fluorescent albumin uptake by 8505c cells pre-treated for 5h with 50μM or 100μM EIPA, which is known to block macropinocytosis (n≥126 cells per cond., data are means ± s.e., using one-way ANOVA/Dunnett).

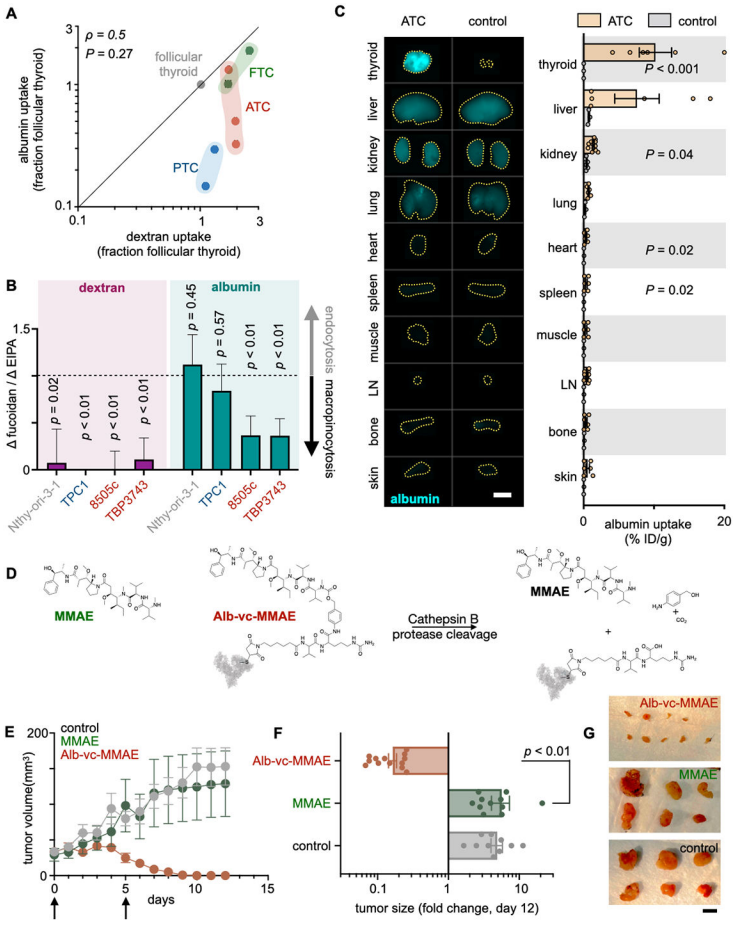

Figure 2. ATC tumors accumulate serum albumin and respond to albumin-drug-conjugate.

A, Correlation between dextran and albumin uptake across thyroid cell lines, as measured by microscopy. Data are means ± s.e. for each cell line from n≥90 total cells (follicular thyroid = Nthy-ori-3-1). Spearman rank correlation ρ and corresponding *P* value are shown. **B**, The ratio of fucoidan inhibition versus EIPA inhibition of dextran or albumin uptake in follicular thyroid (grey), PTC (blue), and ATC (red) cells. Data are means ± s.e., one-way ANOVA/ Tukey (n=9 images / condition). **C**, Representative fluorescent reflectance images (scale bar, 5 mm) and quantification of 15mg/kg fluorescent albumin in B6129SF1/J mice bearing TBP3743 tumors (n=6), and tumor-free mice (n=3), 24h after i.v. administration. Data are means ± s.e., using two-tailed t test; percentage of injected dose per gram tissue, %ID/g; lymph node, LN. **D,** Scheme of cathepsin-mediated MMAE release from Alb-vc-MMAE (Alb structure, PDB 1E78). **E-G**, TBP3743 tumor growth following treatment (arrows; 1μmol/kg MMAE) measured by caliper and plotted according to average volume (**E**) or as individual tumors (**F-G**). N≥10 tumors per group, data are means ± s.e., one-way ANOVA/ Tukey compared to MMAE, scale bar 5 mm.

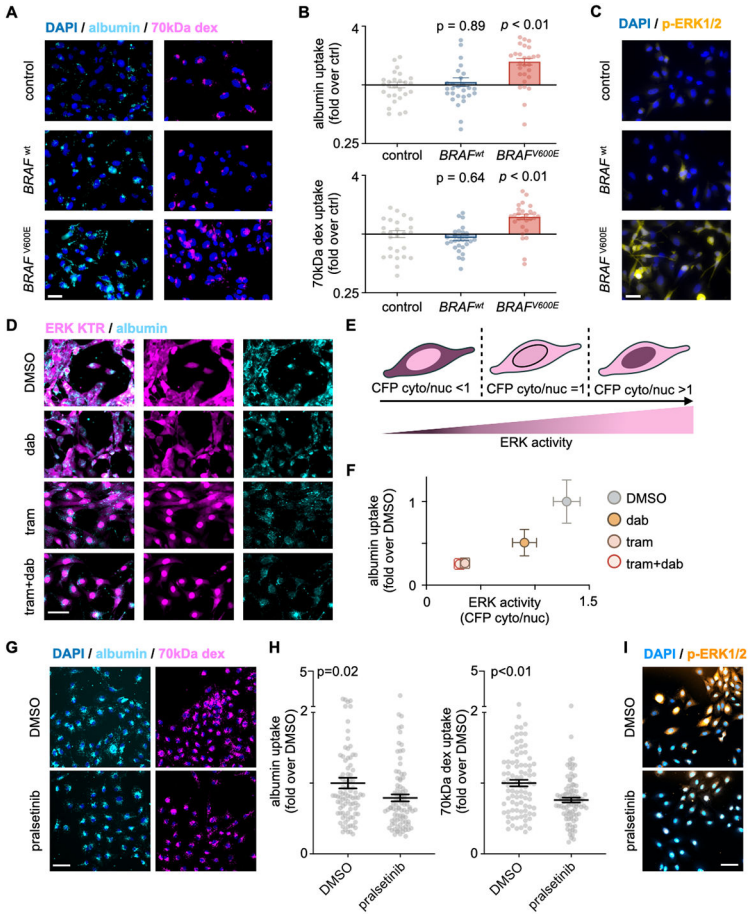

Figure 3. Serum albumin uptake depends on MAPK/ERK activity.

A-B, Representative images (**A**, scale bar, 50μm) and quantification (**B**) of Nthy-ori-3-1 cells transfected with empty vector (control), *BRAF*^{wt} or *BRAF*^{V600E} plasmid for 72h prior to 4h albumin and dextran administration and subsequent microscopy. Data are means ± s.e., n=27 images from 3 experiments, using one-way ANOVA/Dunnett compared to control. **C**, Representative p-ERK1/2 immunofluorescence (scale bar, 50μm) matching conditions in **A**. **D-F**, Representative images (**D**, scale bar, 50μm), ERK kinase translocation reporter schematic (**E**), and quantification (**F**, n=9 images across all cond., means ± s.e.) of 4h albumin uptake in TBP3743 cells pretreated with dabrafenib, trametinib, or the combination for 24h. **G-H**, Representative images (**G**, scale bar, 50μm) and quantification (**H**) of TPC1 cells treated with 50nM pralsetinib for 24h prior to 4h albumin and dextran. Data are means ± s.e., n=90 cells, using two-tailed t-test. **I**, Representative immunofluorescence (scale bar, 50μm) of p-ERK1/2 matching conditions in **G**.

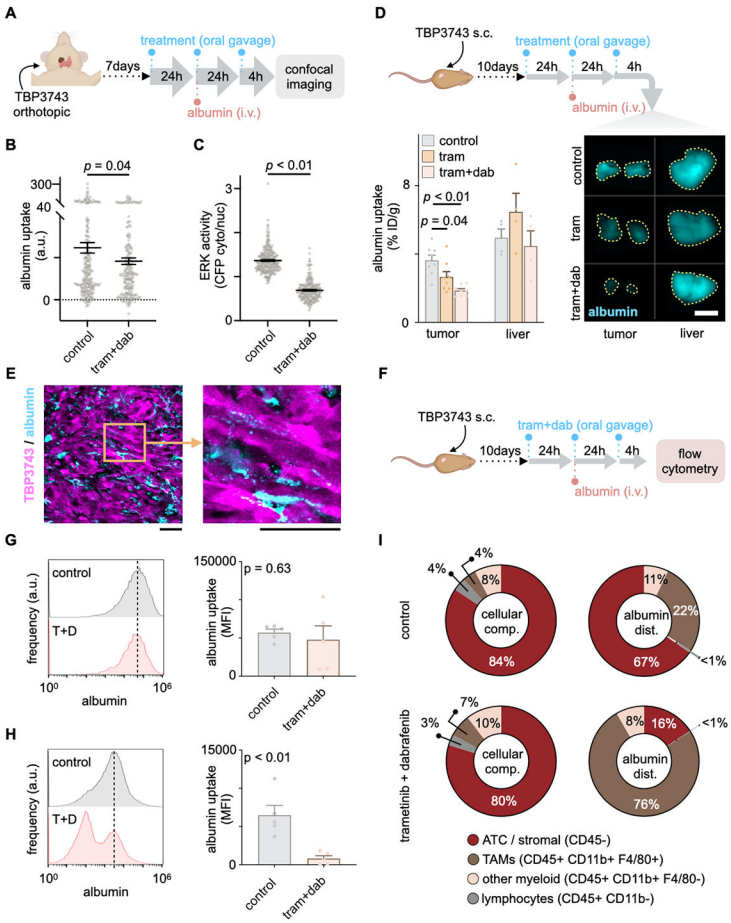

Figure 4. BRAF and MEK kinase inhibition reduces albumin uptake in ATC cancer cells but not tumor-associated macrophages (TAMs).

A-C, Experimental scheme (**A**) and quantification of single-cell albumin uptake (**B**) and ERK activity (**C**) using confocal microscopy of fluorescent albumin and the ERK kinase translocation reporter, in n≥209 TBP3743 cells from 4 mice per cond. Data are means ± s.e., using two-tailed t-tests. **D**, Experimental schematic (top), representative fluorescence reflectance images (bottom right; scale bar, 5mm) and quantification (bottom left) of albumin uptake. Data are means ± s.e. from n=4 mice per group, using one-way ANOVA/ Tukey. **E**, Representative confocal microscopy shows the distribution of fluorescent albumin (cyan) in mTurqoise+ TBP3743 tumors (magenta), 24h post-administration (scale bar, 50μm). **F**, Experimental schematic for *G-I*. **G-I**, Flow cytometry of fluorescent albumin shown as single-cell distributions (left) and as averaged across tumors (right), in CD11b+ F4/80+ TAMs (**G**) and CD45− ATC/stromal cells (**H**). **I,** Flow cytometry of cellular tumor composition (left), and partitioning of fluorescent albumin (right); n=5 per cond., data are means ± s.e., using two-tailed t-tests. Schematics created with BioRender.com.

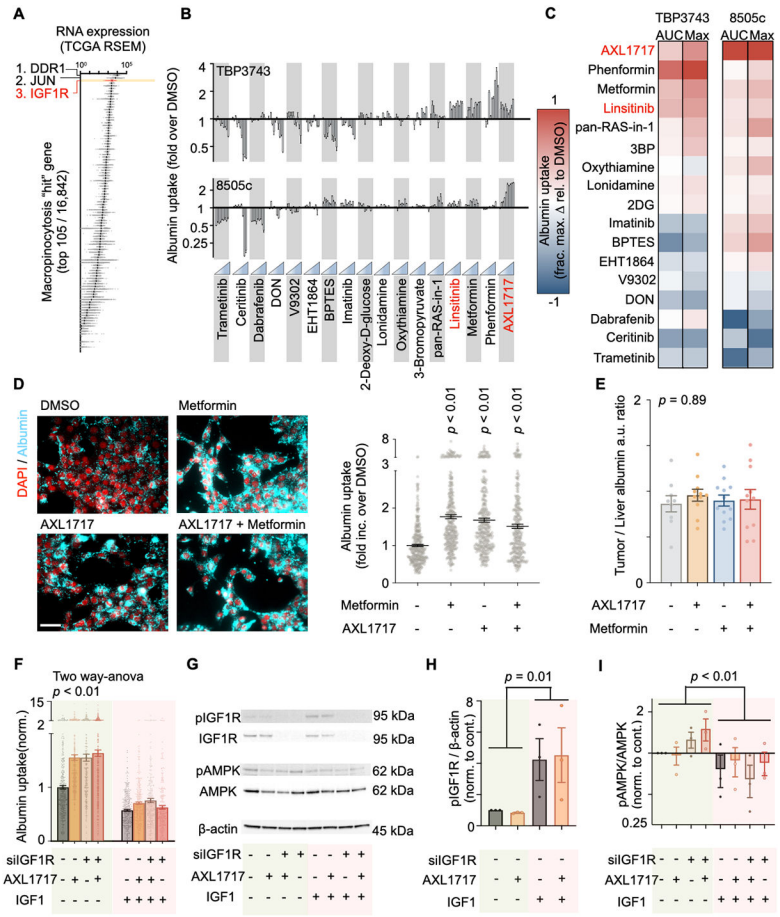

Figure 5. IGF1R-targeted kinase inhibition enhances albumin uptake and is reversed by IGF1.

A, RNA expression from n=397 thyroid tumors was ranked among the top 105 hits from a genome-wide macropinocytosis screen (40). **B-C**, Flow cytometry of 4 h fluorescent albumin uptake in ATC cells across a dose-response of 24 h drug pre-treatment (**B**, means ± s.e., n = 3) and their max and area under the curve (AUC) (**C).** 6-Diazo-5-oxo-L-norleucine (DON). IGF1R-targeted inhibitors are highlighted red. **D**, Representative images (scale bar, 50μm) and quantification (means ± s.e., one-way ANOVA/Tukey) of 4 h albumin uptake by TBP3743 pretreated with DMSO, metformin and/or AXL1717 for 24 h (n ≥ 294 cells across all cond.). **E**, Tumor to liver albumin biodistribution ratio of TBP3743 tumor-bearing mice treated with AXL1717, metformin or the combination (means ± s.e., one-way ANOVA, n≥9 tumors across all cond.). **F-I**, 8505c cells were treated with IGF1R-targeted pooled siRNA or control siRNA for 48 h, followed by AXL1717 or DMSO for 24h, ± IGF1 for another 4 h. **F**, Microscopy quantification (means ± s.e. from n ≥ 231 cells per cond.; two-way ANOVA) of 4 h albumin uptake. **G-H**, Representative western blots (**G**) of p-AMPKα(Thr172) and total AMPK, p-IGF1R (Tyr1135) and total IGF1R, and β-actin, along with ratiometric quantification (**H-I**; means ± s.e., n=3 per cond.; two-way ANOVA).

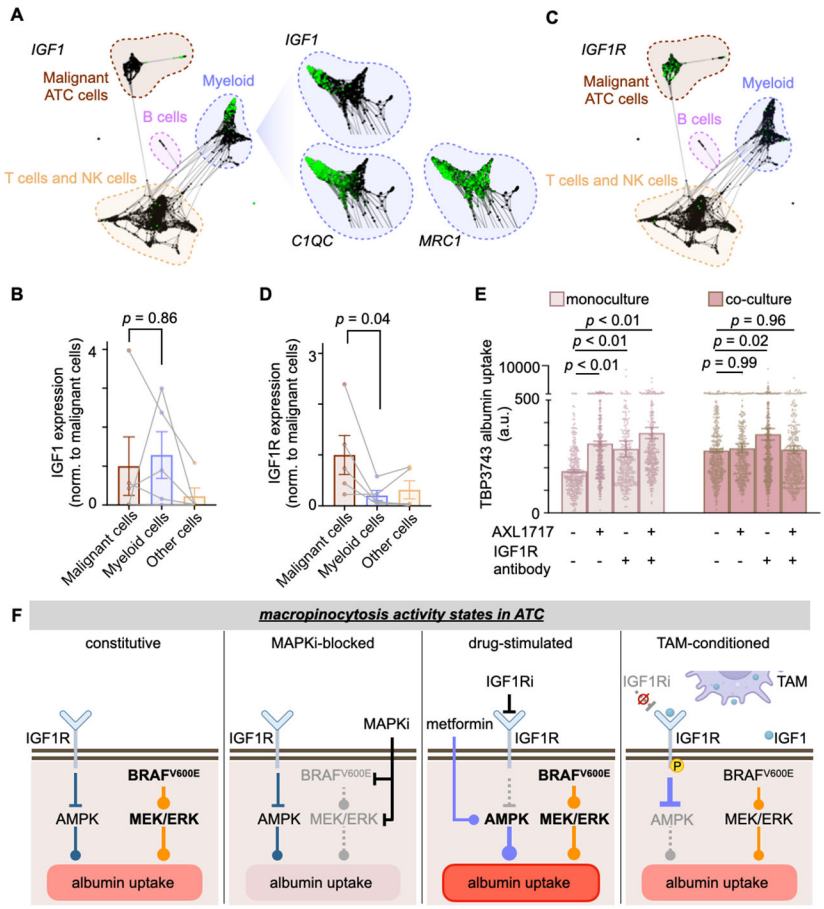

Figure 6. Macrophages limit IGF1R inhibition effects in ATC cells.

A and C, Representative expression of *IGF1* (**A**) and *IGF1R* (**C**) in a patient ATC tumor by SPRING visualization of single-cell RNA-sequencing (scRNAseq) data, shown with individual cells colored green according to gene expression. **B and D**, Relative scRNAseq expression of *IGF1* (**B**) and *IGF1R* (**D**) in myeloid versus malignant cells; datapoints correspond to individual patient samples, shown as means ± s.e. across n=5; one-way ANOVA/Dunnett compared to malignant cells. **E**, AXL1717 increased TBP3743 cell uptake of fluorescent albumin in monoculture but not when co-cultured with interleukin-4 (IL-4) induced bone marrow derived macrophages after 4 h treatment (means ± s.e. from n ≥ 304 cells per cond.; one-way ANOVA/Dunnett). **F**, Summary of albumin uptake in *BRAF*^{V600E} ATC. MAPK inhibition (MAPKi) via dabrafenib and trametinib reduces albumin uptake; IGF1R inhibition (IGF1Ri) and metformin enhance uptake by stimulating AMPK; IGF1 secreted by tumor associated macrophages (TAM) blocks IGF1Ri effects.